

# Dijet bounds on third-generation four-quark operators

---

Maximilian Freiheit<sup>a</sup> and Ulrich Haisch<sup>a</sup>

<sup>a</sup>*Max Planck Institute for Physics,  
Boltzmannstr. 8, 85748 Garching, Germany*

*E-mail:* [maximilian.freiheit@mpp.mpg.de](mailto:maximilian.freiheit@mpp.mpg.de), [haisch@mpp.mpg.de](mailto:haisch@mpp.mpg.de)

**ABSTRACT:** We use dijet measurements from the Large Hadron Collider to constrain ten third-generation four-quark operators in the Standard Model effective field theory. At tree level, only the five operators involving four bottom quarks are directly constrained, but renormalization group (RG) effects allow all ten operators to be probed. Our analysis includes the dominant leading-logarithmic RG contributions up to two-loop order. The resulting bounds for the first five operators are nominal stronger or comparable to current limits, while those for the remaining operators remain weak despite the inclusion of logarithmically enhanced corrections.

---

## Contents

<b>1</b>	<b>Introduction</b>	<b>1</b>
<b>2</b>	<b>Theoretical framework</b>	<b>2</b>
<b>3</b>	<b>Anatomy of dijet constraints</b>	<b>2</b>
<b>4</b>	<b>Phenomenology</b>	<b>6</b>
<b>5</b>	<b>Conclusions</b>	<b>10</b>

---

## 1 Introduction

One idea that has stood the test of time since 1985 is the concept of an effective Lagrangian for new interactions and flavor conservation [1]. Today, this framework is known as the Standard Model effective field theory (SMEFT) [2–4] and has become a central tool for probing indirect signatures of physics beyond the Standard Model (BSM) at the Large Hadron Collider (LHC). The increasing precision of experimental measurements calls for equally precise theoretical predictions, both within the Standard Model (SM) and for possible BSM effects.

A notable feature of the SMEFT — sometimes viewed as a bug, sometimes as a feature — is the large number of effective operators and their mixing under the renormalization group (RG) flow [5–26]. Perhaps the most important consequence of the RG evolution is that it inevitably breaks the accidental symmetries of the SM, such as the flavor  $U(3)^5$  or the custodial  $SU(2)$  symmetry. As a result, operators that are only weakly constrained by direct tree-level measurements can, in some cases, be probed indirectly through loop-level observables. A prime example is the purely right-handed top four-quark operator, which induces two-loop double-logarithmic contributions to the  $\rho$  parameter [27–30], a key quantity in electroweak (EW) precision measurements. Similar two-loop double-logarithmic effects also arise in the processes  $gg \rightarrow h$  and  $h \rightarrow \gamma\gamma$  [17, 22], although they are phenomenologically less significant. In this article, we emphasize that two-loop double-logarithmic contributions can mediate mixing from third-generation to first- and second-generation four-quark operators. This effect may be important, as the Wilson coefficients of four-quark operators involving third-generation fermions remain only weakly constrained [22, 30–35]. Consequently, once radiative corrections from RG evolution are included, dijet measurements at the LHC could provide meaningful constraints on these third-generation four-quark operators. Although jet physics has been employed to constrain SMEFT operators [36–43], to our knowledge, constraints specifically on third-generation four-quark operators have not yet been established.

The remainder of this article is organized as follows. In Section 2, we introduce the subset of dimension-six SMEFT operators relevant to our analysis. Section 3 exemplifies the main steps in computing the SMEFT corrections to dijet production. The phenomenological implications of our calculations are discussed in Section 4, and we conclude in Section 5.

## 2 Theoretical framework

To establish our notation and conventions, we begin by defining the SMEFT Lagrangian as

$$\mathcal{L}_{\text{SMEFT}} = \sum_i C_i(\mu_R) Q_i. \quad (2.1)$$

Here,  $C_i(\mu_R)$  denotes the dimensionful Wilson coefficients evaluated at the renormalization scale  $\mu_R$ , which multiply the corresponding effective operators  $Q_i$ . Throughout this work, we assume that all Wilson coefficients are real.

In the Warsaw basis [2], the dimension-six four-quark operators relevant to this work are given by:

$$\begin{aligned} Q_{qq,ijkl}^{(1)} &= (\bar{q}_i \gamma_\mu q_j)(\bar{q}_k \gamma^\mu q_l), & Q_{qq,ijkl}^{(3)} &= (\bar{q}_i \gamma_\mu \sigma^I q_j)(\bar{q}_k \gamma^\mu \sigma^I q_l), \\ Q_{uu,ijkl} &= (\bar{u}_i \gamma_\mu u_j)(\bar{u}_k \gamma^\mu u_l), & Q_{dd,ijkl} &= (\bar{d}_i \gamma_\mu d_j)(\bar{d}_k \gamma^\mu d_l), \\ Q_{ud,ijkl}^{(1)} &= (\bar{u}_i \gamma_\mu u_j)(\bar{d}_k \gamma^\mu d_l), & Q_{ud,ijkl}^{(8)} &= (\bar{u}_i \gamma_\mu T^A u_j)(\bar{d}_k \gamma^\mu T^A d_l), \\ Q_{qu,ijkl}^{(1)} &= (\bar{q}_i \gamma_\mu q_j)(\bar{u}_k \gamma^\mu u_l), & Q_{qu,ijkl}^{(8)} &= (\bar{q}_i \gamma_\mu T^A q_j)(\bar{u}_k \gamma^\mu T^A u_l), \\ Q_{qd,ijkl}^{(1)} &= (\bar{q}_i \gamma_\mu q_j)(\bar{d}_k \gamma^\mu d_l), & Q_{qd,ijkl}^{(8)} &= (\bar{q}_i \gamma_\mu T^A q_j)(\bar{d}_k \gamma^\mu T^A d_l). \end{aligned} \quad (2.2)$$

The symbol  $q$  denotes the left-handed quark  $SU(2)_L$  doublets, while  $u$  and  $d$  denote the right-handed up- and down-quark  $SU(2)_L$  singlets, respectively. The indices  $i, j, k$ , and  $l$  represent flavor indices in the weak eigenstate basis. The symbols  $\sigma^I$  denote the Pauli matrices, and  $T^A = \lambda^A/2$  are the  $SU(3)_C$  generators, with  $\lambda^A$  representing the Gell-Mann matrices. Of particular interest in what follows are the third-generation four-quark operators, i.e., the operators in (2.2) with  $i = j = k = l = 3$ . These operators will be denoted by  $Q_{QQ}^{(1)}$ ,  $Q_{QQ}^{(3)}$ ,  $Q_{tt}$ ,  $Q_{bb}$ ,  $Q_{tb}^{(1)}$ ,  $Q_{tb}^{(8)}$ ,  $Q_{Qt}^{(1)}$ ,  $Q_{Qt}^{(8)}$ ,  $Q_{Qb}^{(1)}$ , and  $Q_{Qb}^{(8)}$ . Before proceeding, we note that in the phenomenological analysis of Section 4, all quark Yukawa couplings except that of the top quark are set to zero. Moreover, the Cabibbo-Kobayashi-Maskawa matrix is taken to be diagonal when transforming the quark fields from the weak to the mass eigenstate basis.

## 3 Anatomy of dijet constraints

In this section, we outline the essential ingredients and calculations needed to use searches for light jet pairs to constrain the Wilson coefficients of the third-generation four-quark operators introduced in (2.2). The observable of interest is the dijet angular distribution, i.e.,

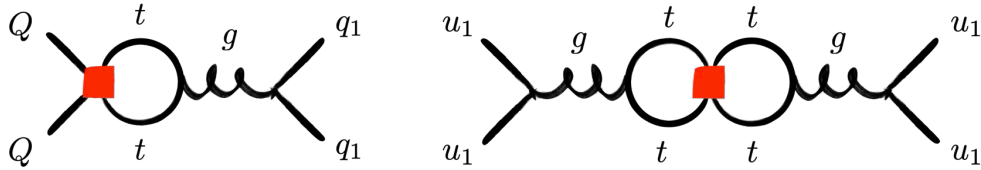


**Figure 1.** Left: Example of a QCD penguin diagram. Right: Example of a QCD double-penguin diagram. The red boxes indicate operator insertions. The leading UV poles of these diagrams determine, respectively, the one-loop logarithmic and two-loop double-logarithmic corrections in the SMEFT RG flow of the third-generation four-quark operators. See main text for more details.

the differential cross section for a pair of jets with invariant mass  $M_{jj}$  produced at an angle  $\hat{\theta}$  relative to the beam direction in the jet-jet center-of-mass (CM) frame.

Unlike conventional resonance searches, the dijet angular distribution provides the advantage of constraining broad  $s$ -channel resonances or modifications of the spectrum arising from higher-dimensional operators in a relatively model-independent manner. This is because the dominant channels in QCD dijet production follow the familiar Rutherford scattering behavior,

$$\frac{d\sigma}{d\cos\hat{\theta}} \propto \frac{1}{\sin^4(\hat{\theta}/2)}, \quad (3.1)$$

at small angles  $\hat{\theta}$ , characteristic of  $t$ -channel exchange of a massless spin-1 boson. To regularize the Rutherford singularity, one commonly studies dijet cross sections differential in

$$\chi = \frac{1 + \cos\hat{\theta}}{1 - \cos\hat{\theta}}. \quad (3.2)$$

In the small-angle limit,  $\chi \rightarrow \infty$ , the partonic differential QCD cross section becomes approximately constant,

$$\frac{d\sigma}{d\chi} \propto \text{const.} \quad (3.3)$$

The presence of a heavy resonance or an effective operator can induce additional hard scatterings, resulting in increased jet production perpendicular to the beam. As a consequence, one expects deviations from the QCD prediction, manifested as enhanced high-energy jet activity in the central region of the detector. In particular, if the angular distributions are influenced by a heavy degree of freedom or an effective operator, an excess of events is expected in  $d\sigma/d\chi$  for  $\chi \rightarrow 1$  at large  $M_{jj}$ , relative to the approximately flat QCD background. In contrast, heavy BSM physics is not expected to leave a significant imprint in the  $d\sigma/d\chi$  distribution for  $\chi \rightarrow \infty$ .

The above discussion is best illustrated with simple examples relevant to this analysis. We first note that, owing to the proton's nonzero bottom-quark parton distribution function (PDF) in the five-flavor scheme, all third-generation four-quark operators with four bottom quarks contribute at tree level to dijet production at the LHC. In the notation introduced in the previous section, these are the five operators  $Q_{QQ}^{(1)}$ ,  $Q_{QQ}^{(3)}$ ,  $Q_{bb}$ ,  $Q_{Qb}^{(1)}$ , and  $Q_{Qb}^{(8)}$ .

In the case of the operator  $Q_{Qb}^{(8)}$ , and assuming massless bottom quarks, the squared matrix element for tree-level  $bb \rightarrow bb$  scattering, including the pure SM contribution, is, for example, given by

$$\begin{aligned} \overline{\sum} |\mathcal{M}(bb \rightarrow bb)|^2 = & \frac{256\pi^2 \alpha_s^2(M_{jj}) (3\chi^4 + 2\chi^3 + \chi^2 + 2\chi + 3)}{27\chi^2 (\chi + 1)^2} \\ & - \frac{64\pi \alpha_s(M_{jj}) M_{jj}^2 (\chi^2 - \chi + 1)}{9\chi (\chi + 1)^2} C_{Qb}^{(8)}(M_{jj}) \\ & + \frac{8M_{jj}^4 (\chi^2 + 1)}{9(\chi + 1)^4} (C_{Qb}^{(8)}(M_{jj}))^2. \end{aligned} \quad (3.4)$$

Here, the symbol  $\overline{\sum}$  indicates that the color and spin indices are averaged over the initial states and summed over the final states, while  $\alpha_s = g_s^2/(4\pi)$  denotes the QCD coupling constant. As seen from (3.4), the terms linear and quadratic in  $C_{Qb}^{(8)}$  are enhanced by two and four powers of the dijet invariant mass, respectively, relative to the SM contribution, reflecting the higher-dimensional nature of the effective interactions introduced in (2.2). The renormalization scale in both  $\alpha_s$  and  $C_{Qb}^{(8)}$  has been set to  $M_{jj}$  in (3.4), which represents the natural choice. Apart from  $Q_{Qb}^{(1)}$ , which does not interfere with the SM due to its color structure, the squared matrix elements of  $Q_{QQ}^{(1)}$ ,  $Q_{QQ}^{(3)}$ , and  $Q_{bb}$  have the same structure as above. Similar considerations apply to  $b\bar{b} \rightarrow b\bar{b}$  scattering.

Since the five-flavor scheme lacks a top-quark PDF and dijet searches do not involve top quarks in the final state, the top-quark counterpart  $Q_{Qt}^{(8)}$  of the operator  $Q_{Qb}^{(8)}$  does not contribute to dijet production at tree level. However, if matching to a ultraviolet (UV) complete model at the scale  $\Lambda$  generates a nonzero Wilson coefficient  $C_{Qt}^{(8)}(\Lambda)$ , the one-loop RG flow in the SMEFT will induce, at the scale  $M_{jj}$ , nonzero Wilson coefficients for four-quark operators with first- or second-generation content that contribute to dijet production at tree level. At leading-logarithmic (LL) accuracy, the relevant one-loop corrections are

$$\begin{aligned} \frac{C_{qq,ii33}^{(1)}(M_{jj})}{C_{Qt}^{(8)}(\Lambda)} &\simeq \frac{\alpha_s(\Lambda)}{72\pi} L, & \frac{C_{qq,i33i}^{(1)}(M_{jj})}{C_{Qt}^{(8)}(\Lambda)} &\simeq -\frac{\alpha_s(\Lambda)}{48\pi} L, & \frac{C_{qq,i33i}^{(3)}(M_{jj})}{C_{Qt}^{(8)}(\Lambda)} &\simeq -\frac{\alpha_s(\Lambda)}{48\pi} L, \\ \frac{C_{qu,33ii}^{(8)}(M_{jj})}{C_{Qt}^{(8)}(\Lambda)} &\simeq -\frac{\alpha_s(\Lambda)}{6\pi} L, & \frac{C_{qd,33ii}^{(8)}(M_{jj})}{C_{Qt}^{(8)}(\Lambda)} &\simeq -\frac{\alpha_s(\Lambda)}{6\pi} L, \end{aligned} \quad (3.5)$$

where  $i = 1, 2$  and we have introduced the abbreviation  $L = \ln(\Lambda/M_{jj})$ . The results in (3.5) can be derived from the SMEFT anomalous dimensions computed in [7]. In the language of flavor physics, the relevant anomalous dimensions result from QCD penguin insertions. An example diagram is shown on the left-hand side of Figure 1. The corrections in (3.5) therefore induce logarithmically enhanced one-loop contributions to the squared matrix element relevant for dijet production. For instance, in the case of  $bd \rightarrow bd$  scattering, the

squared matrix element resulting from (3.5), including the SM contribution, takes the form:

$$\begin{aligned} \overline{\sum} |\mathcal{M}(bd \rightarrow bd)|^2 &\simeq \frac{128\pi^2 \alpha_s^2(M_{jj}) (2\chi^2 + 2\chi + 1)}{9(\chi + 1)^2} \\ &+ \frac{16\alpha_s(M_{jj})\alpha_s(\Lambda)M_{jj}^2 (2\chi^2 + 2\chi + 1)}{27(\chi + 1)^3} LC_{Qt}^{(8)}(\Lambda) \\ &+ \frac{\alpha_s^2(\Lambda)M_{jj}^4 (2\chi^2 + 2\chi + 1)}{81\pi^2(\chi + 1)^4} (LC_{Qt}^{(8)}(\Lambda))^2. \end{aligned} \quad (3.6)$$

Similar considerations apply to the other relevant partonic  $2 \rightarrow 2$  scattering processes.

Unlike the third-generation four-quark operators  $Q_{QQ}^{(1)}$ ,  $Q_{QQ}^{(3)}$ ,  $Q_{bb}$ ,  $Q_{tb}^{(1)}$ ,  $Q_{tb}^{(8)}$ ,  $Q_{Qt}^{(1)}$ ,  $Q_{Qt}^{(8)}$ ,  $Q_{Qb}^{(1)}$ , and  $Q_{Qb}^{(8)}$ , the purely right-handed top four-quark operator  $Q_{tt}$  does not induce logarithmically enhanced one-loop corrections in dijet production. This is intuitively clear, since converting two top-quark currents into two light-quark currents requires a double-penguin operator insertion. The right side of Figure 1 presents an example of such a diagram. As a result of this two-step mixing process, one, however, obtains double-logarithmic two-loop corrections. See, for instance, [17, 44] for recent discussions, including a resummation of such effects. At LL accuracy, the relevant two-loop corrections inducing purely first- or second-generation four-quark operators are

$$\begin{aligned} \frac{C_{qq,iiii}^{(1)}(M_{jj})}{C_{tt}(\Lambda)} &\simeq \frac{9\alpha_s^2(\Lambda) + 32\alpha_1^2(\Lambda)}{1944\pi^2} L^2, & \frac{C_{qq,iiii}^{(3)}(M_{jj})}{C_{tt}(\Lambda)} &\simeq \frac{\alpha_s^2(\Lambda)}{72\pi^2} L^2, \\ \frac{C_{uu,iiii}(M_{jj})}{C_{tt}(\Lambda)} &\simeq \frac{9\alpha_s^2(\Lambda) + 128\alpha_1^2(\Lambda)}{486\pi^2} L^2, & \frac{C_{dd,iiii}(M_{jj})}{C_{tt}(\Lambda)} &\simeq \frac{9\alpha_s^2(\Lambda) + 32\alpha_1^2(\Lambda)}{486\pi^2} L^2, \\ \frac{C_{qu,iiii}^{(1)}(M_{jj})}{C_{tt}(\Lambda)} &\simeq \frac{32\alpha_1^2(\Lambda)}{243\pi^2} L^2, & \frac{C_{qu,iiii}^{(8)}(M_{jj})}{C_{tt}(\Lambda)} &\simeq \frac{\alpha_s^2(\Lambda)}{9\pi^2} L^2, \\ \frac{C_{qd,iiii}^{(1)}(M_{jj})}{C_{tt}(\Lambda)} &\simeq -\frac{16\alpha_1^2(\Lambda)}{243\pi^2} L^2, & \frac{C_{qd,iiii}^{(8)}(M_{jj})}{C_{tt}(\Lambda)} &\simeq \frac{\alpha_s^2(\Lambda)}{9\pi^2} L^2, \\ \frac{C_{ud,iiii}^{(1)}(M_{jj})}{C_{tt}(\Lambda)} &\simeq -\frac{64\alpha_1^2(\Lambda)}{243\pi^2} L^2, & \frac{C_{ud,iiii}^{(8)}(M_{jj})}{C_{tt}(\Lambda)} &\simeq \frac{\alpha_s^2(\Lambda)}{9\pi^2} L^2. \end{aligned} \quad (3.7)$$

Here, again,  $i = 1, 2$ , and we have introduced  $\alpha_1 = g_1^2/(4\pi)$ , with  $g_1$  denoting the  $U(1)_Y$  gauge coupling. It is relatively straightforward to derive the results (3.7) from the SMEFT anomalous dimensions computed in [7]. Notice that some of the Wilson coefficients at  $M_{jj}$  are induced by QED double-penguin insertions, due to the color structure of the corresponding operators. Using (3.7), one can compute the induced LL-enhanced two-loop contributions to the squared matrix element relevant for dijet production. In the case of  $uu \rightarrow uu$  scattering, we find, for example, the following expression for the full SM plus BSM contri-

bution arising from a nonzero initial condition  $C_{tt}(\Lambda)$ :

$$\begin{aligned} \overline{\sum} |\mathcal{M}(uu \rightarrow uu)|^2 \simeq & \frac{256\pi^2 \alpha_s^2(M_{jj}) (3\chi^4 + 2\chi^3 + \chi^2 + 2\chi + 3)}{27\chi^2 (\chi + 1)^2} \\ & - \frac{64\alpha_s(M_{jj}) \alpha_s^2(\Lambda) M_{jj}^2 (5\chi^2 + \chi + 5)}{243\pi \chi (\chi + 1)^2} L^2 C_{tt}(\Lambda) \\ & + \frac{8\alpha_s^4(\Lambda) M_{jj}^4 (7\chi^2 + 8\chi + 7)}{2187\pi^4 (\chi + 1)^4} (L^2 C_{tt}(\Lambda))^2. \end{aligned} \quad (3.8)$$

Here, for simplicity, we have dropped subleading terms involving powers of  $\alpha_1$ . The structure of the squared matrix elements for the other relevant  $2 \rightarrow 2$  channels is similar to that shown in (3.8).

The previous discussion has shown that including RG effects induces logarithmically enhanced loop contributions to dijet production associated with third-generation four-quark operators that do not contribute at tree level. To assess whether this observation can be phenomenologically relevant, it is important to recall that, in order to calculate the differential dijet cross sections, one requires not only the squared matrix elements but also the parton-parton luminosities, defined as

$$\mathcal{L}_{ij}(\tau, \mu_F) = \frac{2}{1 + \delta_{ij}} \int_{\tau}^1 \frac{dx}{x} f_{i/p}(x, \mu_F) f_{j/p}\left(\frac{\tau}{x}, \mu_F\right). \quad (3.9)$$

Here,  $\tau = M_{jj}^2/s$ , where  $s$  is the CM energy of the collider, and  $f_{i/p}(x, \mu_F)$  denotes the universal, non-perturbative PDF describing the probability of finding parton  $i$  inside the proton ( $p$ ) with longitudinal momentum fraction  $x$ , while  $\mu_F$  is the factorization scale. Numerically, we find  $\mathcal{L}_{bd}/\mathcal{L}_{bb} \in [2 \cdot 10^2, 1 \cdot 10^3]$  and  $\mathcal{L}_{uu}/\mathcal{L}_{bb} \in [3 \cdot 10^3, 2 \cdot 10^5]$  for the relevant  $\tau$  values. These numbers should be compared to the suppression factor of about  $\alpha_s/(4\pi)L \simeq 7 \cdot 10^{-3}$  per loop, suggesting that the PDF enhancement of the quantum corrections (3.6) and (3.8) could at least partially overcome their loop suppression. To assess the effectiveness of this enhancement mechanism, however, a more detailed study is required. This will be carried out in the next section.

## 4 Phenomenology

To constrain the Wilson coefficients of the third-generation four-quark operators  $Q_{QQ}^{(1)}$ ,  $Q_{QQ}^{(3)}$ ,  $Q_{tt}$ ,  $Q_{bb}$ ,  $Q_{tb}^{(1)}$ ,  $Q_{tb}^{(8)}$ ,  $Q_{Qt}^{(1)}$ ,  $Q_{Qt}^{(8)}$ ,  $Q_{Qb}^{(1)}$ , and  $Q_{Qb}^{(8)}$ , we make use of the CMS dijet analysis [45]. This dataset has also been employed in the previous SMEFT studies [42, 43], and provides dijet angular distributions normalized to unity in seven  $M_{jj}$  ranges, reported as  $1/\sigma d\sigma/d\chi$ , where  $\sigma$  is the relevant dijet cross section within the analysis phase space. Our dijet predictions use CT14nnlo\_as\_0118 PDFs [46], with the renormalization and factorization scales  $\mu_R$  and  $\mu_F$  set to  $M_{jj}$ . These PDFs have also been employed in [45] and are accessed in our computations through `ManeParse` [47]. Our normalized  $1/\sigma d\sigma/d\chi$  distributions are multiplied by a bin-wise  $K$ -factor, defined as the ratio of the CMS SM prediction to our

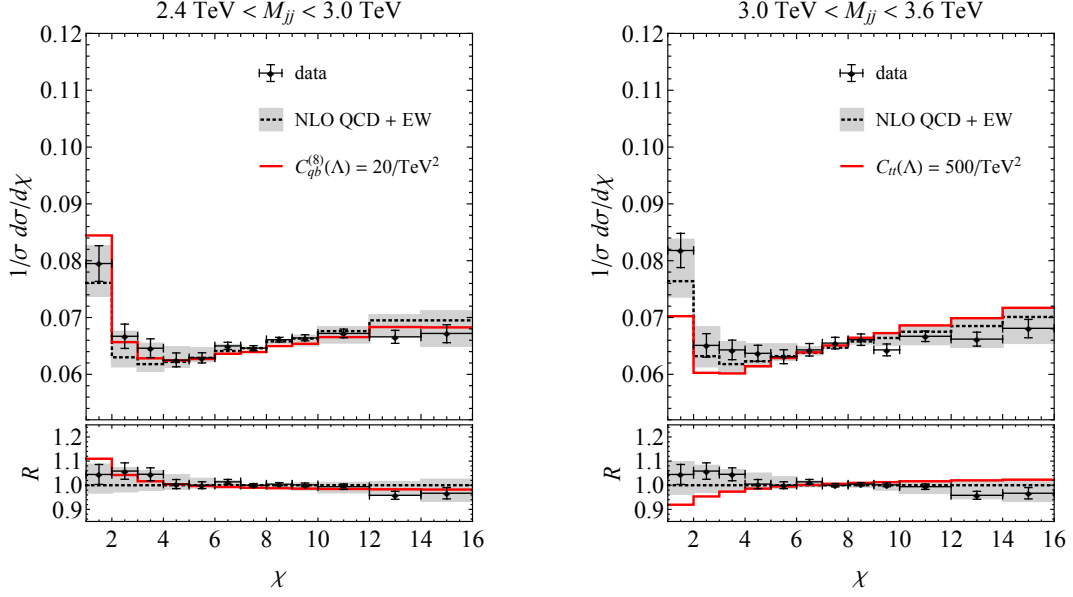


**Figure 2.** Normalized  $\chi$  distributions in the two lowest mass bins considered in the CMS analysis [45]. The SM predictions obtained by CMS, including NLO QCD and EW corrections, are shown as black dotted lines. Error bars denote the statistical and experimental systematic uncertainties added in quadrature, while the gray band represents the theoretical uncertainties. For comparison, the normalized dijet angular distributions for  $C_{qb}^{(8)}(\Lambda) = 20/\text{TeV}^2$  and  $C_{tt}(\Lambda) = 500/\text{TeV}^2$  are shown as red lines in the left- and right-hand panels, respectively. The lower panels display the ratios ( $R$ ) of the unfolded data to the SM predictions, together with the corresponding BSM distributions. Additional explanations can be found in the main text.

leading-order (LO) SM prediction, to account for higher-order perturbative corrections, parton shower (PS) effects, analysis cuts, and detector resolution. The resulting  $K$ -factors lie in the range of about  $[0.95, 1.30]$ , indicating good agreement between our LO SM calculation and the more sophisticated SM prediction obtained by CMS. Applying the same  $K$ -factor to both QCD and BSM results assumes that, for example, PS and detector effects depend only on  $M_{jj}$  and  $\chi$ , not on specific features of the BSM signal — a reasonable assumption, though testing it would require a fully realistic Monte Carlo simulation, which is beyond the scope of this work.

In Figure 2, we present the  $1/\sigma d^2\sigma/d\chi dM_{jj}$  distributions for the two lowest  $M_{jj}$  regions considered by the CMS collaboration in [45], namely  $2.4 \text{ TeV} < M_{jj} < 3.0 \text{ TeV}$  and  $3.0 \text{ TeV} < M_{jj} < 3.6 \text{ TeV}$ . Unfolded data are compared to the SM prediction including next-to-leading order (NLO) QCD and EW corrections (black dotted lines) as calculated by the CMS collaboration. The error bars represent the combined statistical and experimental systematic uncertainties, while theoretical uncertainties are shown as gray bands. For comparison, the normalized dijet angular distributions assuming  $C_{qb}^{(8)}(\Lambda) = 20/\text{TeV}^2$  and  $C_{tt}(\Lambda) = 500/\text{TeV}^2$  are also shown on the left- and right-hand sides, respectively, as red lines. The initial scale is chosen as  $\Lambda = 10 \text{ TeV}$ , and all initial conditions of the third-generation four-quark operators, except for the one indicated in the panel, are set



$C_{QQ}^{(1)}(v)$	$C_{QQ}^{(3)}(v)$	$C_{tt}(v)$	$C_{bb}(v)$	$C_{Qt}^{(1)}(v)$
$[-68, 65]$	$[-58, 61]$	$[-850, 330]$	$[-4.7, 4.7]$	$[-290, 300]$
$C_{Qt}^{(8)}(v)$	$C_{Qb}^{(1)}(v)$	$C_{Qb}^{(8)}(v)$	$C_{tb}^{(1)}(v)$	$C_{tb}^{(8)}(v)$
$[-490, 500]$	$[-6.2, 6.2]$	$[-9.3, 9.4]$	$[-310, 310]$	$[-130, 170]$

**Table 1.** Individual 95% CL limits on the third-generation four-quark operators, derived from the three lowest  $M_{jj}$  bins in the CMS analysis [45] of normalized dijet angular distributions. These limits are obtained from a profiled  $\Delta\chi^2$  analysis and correspond to the Wilson coefficients evaluated at the scale  $v = 250$  GeV. Consult the main text for further details.

to zero. The RG evolution from  $\Lambda$  to  $M_{jj}$  is performed keeping all LL terms up to two loops, including the full dependence on the three SM gauge couplings and the top-quark Yukawa coupling. Both panels clearly show that, as anticipated, the largest relative deviations between the BSM and SM results occur in the lowest bin, where  $\chi \in [1, 2]$ . Note also that for  $C_{Qb}^{(8)}(\Lambda) = 20/\text{TeV}^2$ , the BSM contribution is constructive, as it is dominated by the term quadratic in  $C_{Qb}^{(8)}$ . In contrast, for  $C_{tt}(\Lambda) = 500/\text{TeV}^2$ , one observes destructive interference arising from the term linear in  $C_{tt}$ .

We extract the 95% confidence-level (CL) limits on the Wilson coefficients of the third-generation four-quark operators by performing a  $\chi^2$  fit to the three lowest  $M_{jj}$  bins reported by CMS in [45], spanning  $2.4 \text{ TeV} < M_{jj} < 4.2 \text{ TeV}$ . These bins are chosen because they provide the highest sensitivity to the effects under study once both experimental and theoretical uncertainties are incorporated. In the  $\chi^2$  analysis, all other Wilson coefficients are treated as nuisance parameters and profiled over, thereby accounting for correlations among operators. This procedure yields conservative and robust bounds without assuming that all other coefficients vanish. We have also explicitly checked that profiling produces slightly weaker constraints than marginalization.

One-dimensional constraints are extracted from the profiled  $\chi^2$  by minimizing it and imposing  $\Delta\chi^2 = \chi^2 - \chi_{\min}^2 = 3.84$ . The resulting limits are summarized in Table 1. Note that, for ease of comparison with existing bounds on the Wilson coefficients of third-generation four-quark operators, all quoted ranges refer to the Wilson coefficients evaluated at the EW scale  $v = 250$  GeV. The bounds are derived from the Wilson coefficients at the high scale  $\Lambda = 10$  TeV, obtained from the  $\chi^2$  fit and evolved down to  $v$  using the solutions to the RG equations in the one-loop LL approximation. The calculation of the logarithmically enhanced corrections fully retains the dependence on the three SM gauge couplings as well as the top-quark Yukawa coupling. The RG running effects correspond to relative shifts of 6%, -6%, 24%, 13%, 8%, -7%, 2%, -19%, 3%, and -4% in the order of the Wilson coefficients listed in the table. Overall, Table 1 shows that the direct bounds on the Wilson coefficients of third-generation four-quark operators involving four bottom quarks — namely,  $Q_{QQ}^{(1)}$ ,  $Q_{QQ}^{(3)}$ ,  $Q_{bb}$ ,  $Q_{Qb}^{(1)}$ , and  $Q_{Qb}^{(8)}$  — are significantly stronger than the indirect bounds on the Wilson coefficients of the remaining operators,  $Q_{tt}$ ,  $Q_{Qt}^{(1)}$ ,  $Q_{Qt}^{(8)}$ ,  $Q_{tb}^{(1)}$ , and  $Q_{tb}^{(8)}$ . This demonstrates that the PDF enhancement is not sufficient to overcome the

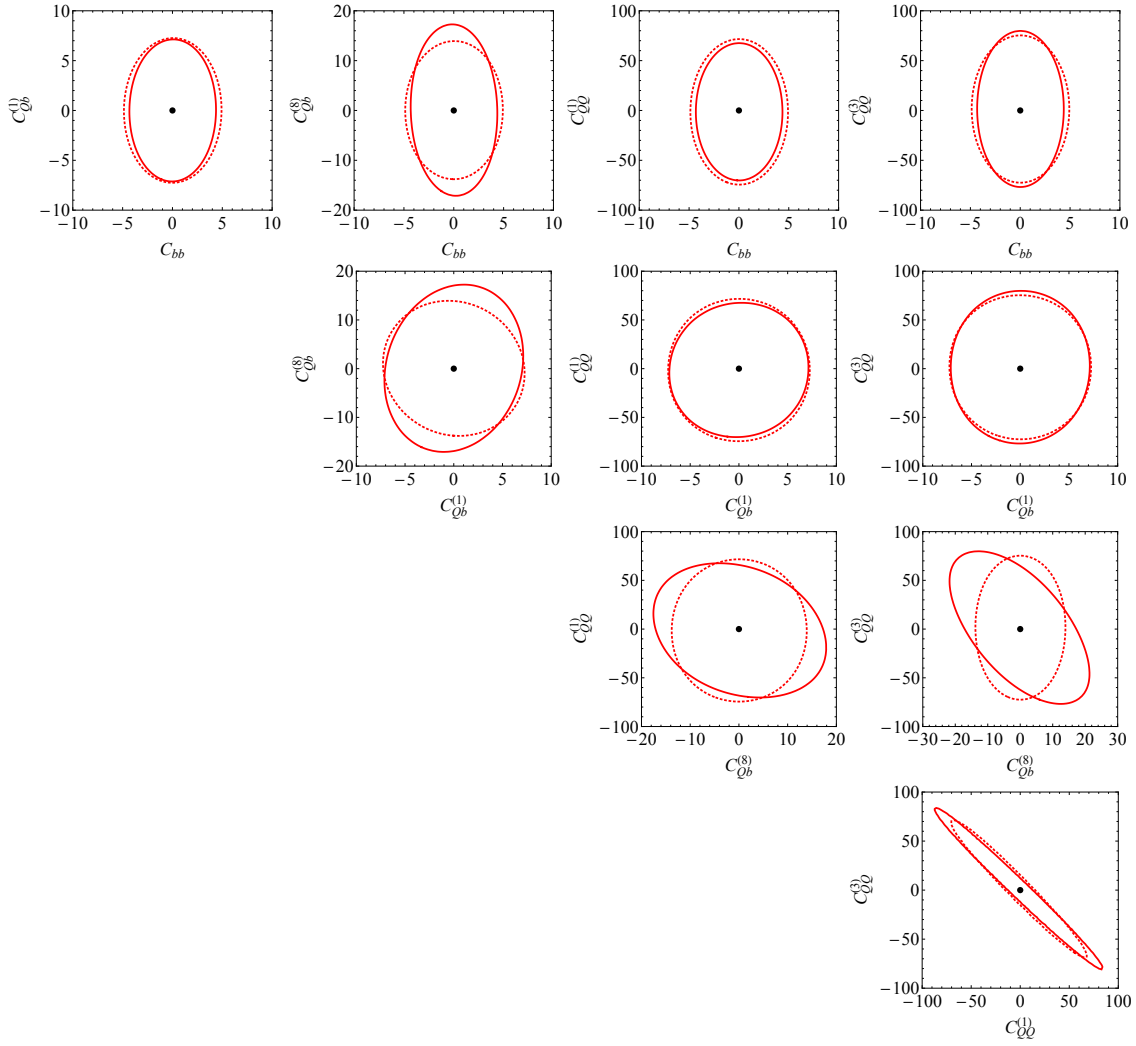


**Figure 3.** 95% CL limits on all possible pairs of third-generation four-quark operators involving four bottom-quark fields. The solid (dotted) red contours show the constraints on the corresponding Wilson coefficients evaluated at  $v = 250$  GeV ( $\Lambda = 10$  TeV). The black point in each of the ten panels represents the SM. Additional details can be found in the main text.

loop suppression of the third-generation four-quark operators, providing only a partial compensation. The most pronounced effect is observed for  $Q_{tb}^{(8)}$ , which receives LL corrections already at the one-loop level, see (3.5).

The 95% CL limits in Table 1 can be compared with similar constraints reported in the literature [22, 30–35]. For  $C_{bb}$ ,  $C_{Qb}^{(1)}$ ,  $C_{Qb}^{(8)}$ ,  $C_{tb}^{(1)}$ , and  $C_{tb}^{(8)}$ , our dijet limits provide, to the best of our knowledge, the most stringent constraints to date, whereas the bounds on  $C_{QQ}^{(1)}$  and  $C_{QQ}^{(3)}$  are generally weaker. This weakness originates from a flat direction in parameter space, roughly along  $C_{QQ}^{(1)} = -C_{QQ}^{(3)}$ , which dijet production cannot effectively lift. Additionally, the limits on  $C_{tt}$ ,  $C_{Qt}^{(1)}$ , and  $C_{Qt}^{(8)}$  are significantly less restrictive than those obtained

from EW precision and top-quark measurements [30, 32–35]. The derived 95% CL limits on  $C_{QQ}^{(1)}$ ,  $C_{QQ}^{(3)}$ ,  $C_{bb}$ ,  $C_{Qt}^{(1)}$ ,  $C_{Qt}^{(8)}$ ,  $C_{Qb}^{(1)}$ ,  $C_{Qb}^{(8)}$ , and  $C_{Qt}^{(1)}$  are approximately symmetric, whereas those on  $C_{tt}$  and  $C_{tb}^{(8)}$  are noticeably asymmetric, indicating that linear contributions in the former set are subdominant but become significant for the latter.

In Figure 3, we present two-dimensional constraints derived from a profiled  $\chi^2$  fit, requiring  $\Delta\chi^2 = \chi^2 - \chi_{\min}^2 = 5.99$ . We focus on the Wilson coefficients  $C_{bb}$ ,  $C_{Qb}^{(1)}$ ,  $C_{Qb}^{(8)}$ ,  $C_{QQ}^{(1)}$ , and  $C_{QQ}^{(3)}$ , which, as discussed above, are the five third-generation four-quark operators most strongly constrained by LHC dijet data. The solid (dotted) red contours indicate the constraints on the Wilson coefficients evaluated at  $v = 250$  GeV ( $\Lambda = 10$  TeV), and the black point in each panel represents the SM. Two features stand out in the figure: the previously mentioned flat direction, approximately along  $C_{QQ}^{(1)} = -C_{QQ}^{(3)}$ , and the noticeable impact of one-loop LL corrections from the SMEFT RG flow on the 95% CL limits. The RG effects are particularly significant for all the pairs of Wilson coefficients involving  $C_{Qb}^{(8)}$  due to the strong QCD mixing of  $Q_{Qb}^{(8)}$  with all the other relevant third-generation four-quark operators. The latter finding shows that properly incorporating RG-induced effects is important when relating LHC and low-energy SMEFT constraints, because the RG running can notably modify the limits on the Wilson coefficients at different energy scales. As in the one-dimensional case, we have explicitly verified that marginalization produces very similar, though slightly stronger, constraints in the planes of Wilson coefficient pairs shown in the ten panels of Figure 3.

## 5 Conclusions

In this article, we have investigated the sensitivity of LHC dijet measurements to the ten third-generation four-quark operators in the SMEFT listed in (2.2). At tree level, only the five operators involving four bottom quarks,  $Q_{QQ}^{(1)}$ ,  $Q_{QQ}^{(3)}$ ,  $Q_{bb}$ ,  $Q_{Qb}^{(1)}$ , and  $Q_{Qb}^{(8)}$ , contribute directly to dijet production. Nevertheless, RG effects that generate logarithmically enhanced contributions allow all ten operators to be probed indirectly when one- and two-loop corrections are included. These contributions stem from QCD and QED penguin diagrams, which mediate flavor-changing effects among the four-quark operators.

Using the normalized dijet angular distributions measured by CMS in [45], we have derived one-dimensional 95% CL limits on the Wilson coefficients of the full set of third-generation four-quark operators. The bounds for operators involving four bottom quarks are relatively strong, often improving upon or comparable to existing limits reported in the literature [22, 30–35]. In contrast, the constraints on the remaining third-generation four-quark operators, which involve only top quarks or both bottom and top quarks, remain comparatively weak and are more effectively probed via EW precision measurements and top-quark observables at the LHC [30, 32–35]. Our findings demonstrate that the enhancement from PDFs, arising from the RG-induced flavor transition from third-generation to first- or second-generation fields, is insufficient to overcome the loop suppression of these operators. For the Wilson coefficients  $C_{QQ}^{(1)}$ ,  $C_{QQ}^{(3)}$ ,  $C_{bb}$ ,  $C_{Qb}^{(1)}$ , and  $C_{Qb}^{(8)}$ , we have also derived two-dimensional constraints for all possible pairs. The analysis shows that RG effects

between the initial scale  $\Lambda$  and the EW scale  $v$  are especially significant for the Wilson-coefficient pairs involving  $C_{Qb}^{(8)}$ . This is driven by the strong QCD mixing of  $Q_{Qb}^{(8)}$  with all other relevant third-generation four-quark operators. This result underscores the importance of including RG-induced contributions when interpreting high-energy LHC data in terms of SMEFT operators, as they can significantly affect the derived constraints at the EW scale.

Due to the high values of the jet-jet invariant mass  $M_{jj}$  probed in LHC dijet analyses, the constraints on the Wilson coefficients of the third-generation four-quark operators derived in this work are generally dominated by the quadratic BSM contributions, with interference between the SM and BSM terms in most cases playing only a subleading role. As a consequence, the derived limits are sensitive to dimension-eight deformations of the SMEFT. This issue, which also affects similar constraints from  $t\bar{t}$  and  $t\bar{t}t\bar{t}$  production at the LHC [32, 34, 35], but not the limits from EW precision measurements [22, 30, 33, 35], should be kept in mind when interpreting the derived bounds in terms of explicit UV complete models.

## Acknowledgments

UH gratefully acknowledges Ben Stefanek, fellow enthusiast of SMEFT double logarithms, for enjoyable discussions. The analytic calculations of the squared matrix elements relevant to this study were performed using `FeynRules` [48], `FeynArts` [49], and `FormCalc` [50], while the beta functions implemented in `DsixTools` 2.0 [51] were used to derive the LL enhanced effects up to the two-loop order.

## References

- [1] W. Buchmüller and D. Wyler, *Nucl. Phys. B* **268**, 621 (1986).
- [2] B. Grzadkowski, M. Iskrzynski, M. Misiak, and J. Rosiek, *JHEP* **10**, 085 (2010), [arXiv:1008.4884 \[hep-ph\]](#).
- [3] I. Brivio and M. Trott, *Phys. Rept.* **793**, 1 (2019), [arXiv:1706.08945 \[hep-ph\]](#).
- [4] G. Isidori, F. Wilsch, and D. Wyler, *Rev. Mod. Phys.* **96**, 015006 (2024), [arXiv:2303.16922 \[hep-ph\]](#).
- [5] E. E. Jenkins, A. V. Manohar, and M. Trott, *JHEP* **10**, 087 (2013), [arXiv:1308.2627 \[hep-ph\]](#).
- [6] E. E. Jenkins, A. V. Manohar, and M. Trott, *JHEP* **01**, 035 (2014), [arXiv:1310.4838 \[hep-ph\]](#).
- [7] R. Alonso, E. E. Jenkins, A. V. Manohar, and M. Trott, *JHEP* **04**, 159 (2014), [arXiv:1312.2014 \[hep-ph\]](#).
- [8] M. Gorbahn and U. Haisch, *JHEP* **10**, 094 (2016), [arXiv:1607.03773 \[hep-ph\]](#).
- [9] Z. Bern, J. Parra-Martinez, and E. Sawyer, *JHEP* **10**, 211 (2020), [arXiv:2005.12917 \[hep-ph\]](#).
- [10] Q. Jin, K. Ren, and G. Yang, *JHEP* **04**, 180 (2021), [arXiv:2011.02494 \[hep-ph\]](#).

- [11] U. Haisch, D. J. Scott, M. Wiesemann, G. Zanderighi, and S. Zanolì, *JHEP* **07**, 054 (2022), [arXiv:2204.00663 \[hep-ph\]](#).
- [12] E. E. Jenkins, A. V. Manohar, L. Naterop, and J. Pagès, *JHEP* **02**, 131 (2024), [arXiv:2310.19883 \[hep-ph\]](#).
- [13] S. Di Noi, R. Gröber, and M. K. Mandal, *JHEP* **12**, 220 (2025), [arXiv:2408.03252 \[hep-ph\]](#).
- [14] L. Born, J. Fuentes-Martín, S. Kvedaraitė, and A. E. Thomsen, *JHEP* **05**, 121 (2025), [arXiv:2410.07320 \[hep-ph\]](#).
- [15] L. Naterop and P. Stoffer, *JHEP* **06**, 007 (2025), [arXiv:2412.13251 \[hep-ph\]](#).
- [16] C. Duhr, A. Vasquez, G. Ventura, and E. Vryonidou, (2025), [arXiv:2503.01954 \[hep-ph\]](#).
- [17] U. Haisch, *JHEP* **06**, 004 (2025), [arXiv:2503.06249 \[hep-ph\]](#).
- [18] D. Zhang, *JHEP* **06**, 106 (2025), [arXiv:2504.00792 \[hep-ph\]](#).
- [19] B. Assi, A. Helset, J. Pagès, and C.-H. Shen, (2025), [arXiv:2504.18537 \[hep-ph\]](#).
- [20] L. Naterop and P. Stoffer, (2025), [arXiv:2507.08926 \[hep-ph\]](#).
- [21] S. Di Noi and R. Gröber, *Phys. Lett. B* **869**, 139878 (2025), [arXiv:2507.10295 \[hep-ph\]](#).
- [22] U. Haisch and M. Niggetiedt, (2025), [arXiv:2507.20803 \[hep-ph\]](#).
- [23] C. Duhr, G. Ventura, and E. Vryonidou, (2025), [arXiv:2508.04500 \[hep-ph\]](#).
- [24] S. Di Noi, B. A. Erdelyi, and R. Gröber, (2025), [arXiv:2510.14680 \[hep-ph\]](#).
- [25] S. Banik, A. Crivellin, L. Naterop, and P. Stoffer, (2025), [arXiv:2510.08682 \[hep-ph\]](#).
- [26] M. Chala and J. López Miras, (2025), [arXiv:2512.04064 \[hep-ph\]](#).
- [27] L. Allwicher, G. Isidori, J. M. Lizana, N. Selimovic, and B. A. Stefanek, *JHEP* **05**, 179 (2023), [arXiv:2302.11584 \[hep-ph\]](#).
- [28] L. Allwicher, C. Cornella, G. Isidori, and B. A. Stefanek, *JHEP* **03**, 049 (2024), [arXiv:2311.00020 \[hep-ph\]](#).
- [29] B. A. Stefanek, *JHEP* **09**, 103 (2024), [arXiv:2407.09593 \[hep-ph\]](#).
- [30] U. Haisch and L. Schnell, *JHEP* **02**, 038 (2025), [arXiv:2410.13304 \[hep-ph\]](#).
- [31] R. Gauld, B. D. Pecjak, and D. J. Scott, *JHEP* **05**, 080 (2016), [arXiv:1512.02508 \[hep-ph\]](#).
- [32] J. J. Ethier, G. Magni, F. Maltoni, L. Mantani, E. R. Nocera, J. Rojo, E. Slade, E. Vryonidou, and C. Zhang (SMEFiT), *JHEP* **11**, 089 (2021), [arXiv:2105.00006 \[hep-ph\]](#).
- [33] S. Dawson and P. P. Giardino, *Phys. Rev. D* **105**, 073006 (2022), [arXiv:2201.09887 \[hep-ph\]](#).
- [34] C. Degrande, R. Rosenfeld, and A. Vasquez, *JHEP* **07**, 114 (2024), [arXiv:2402.06528 \[hep-ph\]](#).
- [35] S. Di Noi, H. El Faham, R. Gröber, M. Vitti, and E. Vryonidou, (2025), [arXiv:2507.01137 \[hep-ph\]](#).
- [36] F. Krauss, S. Kuttimalai, and T. Plehn, *Phys. Rev. D* **95**, 035024 (2017), [arXiv:1611.00767 \[hep-ph\]](#).
- [37] S. Alioli, M. Farina, D. Pappadopulo, and J. T. Ruderman, *JHEP* **07**, 097 (2017), [arXiv:1706.03068 \[hep-ph\]](#).
- [38] S. Alte, M. König, and W. Shepherd, *JHEP* **01**, 094 (2018), [arXiv:1711.07484 \[hep-ph\]](#).

- [39] V. Hirschi, F. Maltoni, I. Tsinikos, and E. Vryonidou, *JHEP* **07**, 093 (2018), [arXiv:1806.04696 \[hep-ph\]](#).
- [40] E. Keilmann and W. Shepherd, *JHEP* **09**, 086 (2019), [arXiv:1907.13160 \[hep-ph\]](#).
- [41] R. Goldouzian and M. D. Hildreth, *Phys. Lett. B* **811**, 135889 (2020), [arXiv:2001.02736 \[hep-ph\]](#).
- [42] U. Haisch and G. Koole, *JHEP* **09**, 133 (2021), [arXiv:2106.01289 \[hep-ph\]](#).
- [43] C. Degrande and M. Maltoni, (2025), [arXiv:2511.04517 \[hep-ph\]](#).
- [44] A. J. Buras and M. Jung, *JHEP* **06**, 067 (2018), [arXiv:1804.05852 \[hep-ph\]](#).
- [45] A. M. Sirunyan *et al.* (CMS), *Eur. Phys. J. C* **78**, 789 (2018), [Erratum: *Eur. Phys. J. C* **82**, 379 (2022)], [arXiv:1803.08030 \[hep-ex\]](#).
- [46] S. Dulat, T.-J. Hou, J. Gao, M. Guzzi, J. Huston, P. Nadolsky, J. Pumplin, C. Schmidt, D. Stump, and C. P. Yuan, *Phys. Rev. D* **93**, 033006 (2016), [arXiv:1506.07443 \[hep-ph\]](#).
- [47] D. B. Clark, E. Godat, and F. I. Olness, *Comput. Phys. Commun.* **216**, 126 (2017), [arXiv:1605.08012 \[hep-ph\]](#).
- [48] A. Alloul, N. D. Christensen, C. Degrande, C. Duhr, and B. Fuks, *Comput. Phys. Commun.* **185**, 2250 (2014), [arXiv:1310.1921 \[hep-ph\]](#).
- [49] T. Hahn, *Comput. Phys. Commun.* **140**, 418 (2001), [arXiv:hep-ph/0012260](#).
- [50] T. Hahn, S. Pačehr, and C. Schappacher, *PoS LL2016*, 068 (2016), [arXiv:1604.04611 \[hep-ph\]](#).
- [51] J. Fuentes-Martin, P. Ruiz-Femenia, A. Vicente, and J. Virto, *Eur. Phys. J. C* **81**, 167 (2021), [arXiv:2010.16341 \[hep-ph\]](#).